Vascular Printing

3D Printing of Aortic Dissections

BACHELORARBEIT

zur Erlangung des akademischen Grades

Bachelor of Science

im Rahmen des Studiums

Medizinische Informatik

eingereicht von

Klaus Eckelt

Matrikelnummer 1127705

an der Fakultät für Informatik

der Technischen Universität Wien

Betreuung: Ao.Univ.Prof. Dipl.-Ing. Dr.techn. Eduard Gröller
Mitwirkung: Dr.techn. Alexey Karimov, MSc

Wien, 31. Jänner 2017

_____   _____
        Klaus Eckelt   Eduard Gröller

Vascular Printing

3D Printing of Aortic Dissections

BACHELOR'S THESIS

submitted in partial fulfillment of the requirements for the degree of

Bachelor of Science

in

Medical Informatics

by

Klaus Eckelt

Registration Number 1127705

to the Faculty of Informatics

at the TU Wien

Advisor: Ao.Univ.Prof. Dipl.-Ing. Dr.techn. Eduard Gröller
Assistance: Dr.techn. Alexey Karimov, MSc

Vienna, 31st January, 2017   _____   _____
                                              Klaus Eckelt   Eduard Gröller

Erklärung zur Verfassung der Arbeit

Klaus Eckelt
Rainerstraße 21/4, 4020 Linz

Hiermit erkläre ich, dass ich diese Arbeit selbständig verfasst habe, dass ich die verwendeten Quellen und Hilfsmittel vollständig angegeben habe und dass ich die Stellen der Arbeit – einschließlich Tabellen, Karten und Abbildungen –, die anderen Werken oder dem Internet im Wortlaut oder dem Sinn nach entnommen sind, auf jeden Fall unter Angabe der Quelle als Entlehnung kenntlich gemacht habe.

Wien, 31. Jänner 2017

_____

Klaus Eckelt

Kurzfassung

Für die Darstellung von Gefäßen gibt es eine Vielzahl von Methoden, wie Curved Planar Reformation (CPR), Curvicircular Feature Aggregation (CFA) oder, die wohl am häufigsten verwendete, Digital Subtraction Angiography (DSA). Je nach zugrundeliegender Krankheit des Patienten wird die am besten geeignete Methode herangezogen. Anstatt die 3-dimensionale Struktur der Gefäße auf einem Bildschirm zu betrachten, wären im klinischen Alltag jedoch oft greifbare Modelle hilfreich. Diese lassen sich einfach zu der täglichen Visite mitnehmen und können für präoperatives Training oder auch zur Orientierung während einer Operation verwendet werden.

In dieser vorliegenden Arbeit werden mehrere Methoden vorgestellt, welche Gefäße in 3D-druckbare Modelle umwandeln. Je nach verfügbarer Information in den Eingangsdaten, können die Gefäße in Röhren mit einem fixen, benutzerdefinierten Durchmesser, in Röhren welche den Durchmesser wie die tatsächlichen Gefäße verändern, oder Eins-zu-eins mittels segmentierter Daten konvertiert werden.

Für die Konvertierung in Röhren kann der Benutzer die Wandstärke und Anzahl der Seiten definieren. Enthält das Gefäßmodell keine Daten zum inneren Durchmesser, kann der Benutzer diesen ebenfalls fixieren.

Im Verlauf der Arbeit wurden fünf 3D-Drucke angefertig und mit digitalen Visualisierungen verglichen. Obwohl lediglich gewöhnliche 3D-Drucker und Materialien verwendet wurden, sind diese preiswerten Drucke, durch die stetige Entwicklung der letzten Jahre, bereits ausreichend, um sich in den genannten Einsatzgebieten als hilfreich zu erweisen.

Abstract

For blood vessels there are plenty of visualization techniques available, like Digital Subtraction Angiography (DSA), Curved Planar Reformation (CPR) and Curvicircular Feature Aggregation (CFA). They are consulted depending on the pathology but have in common that the vessel's 3D structure is viewed on a 2D screen. Tangible solid 3D models would sometimes be a highly appreciated extension in the everyday clinical practice. In comparison to the representations on 2D screens, these models can be easily taken bedside during the doctor's visit, used for pre-operative training or as an intra-operative guidance.

In this thesis, multiple methods that convert vessels to 3D-printable models are presented. Depending on the available information, vessels can be converted to tubes with a user-specified fixed diameter, to tubes that adapt their diameter to the vessel's one, or get turned into 3D-printable models voxel-wise from segmented data.

For tube conversion, the user is provided with the ability to choose wall thickness and number of sides the approximated tube should have. If there is no radii information available, an arbitrary inner radius can be used as well.

Five physical models of vessels were created and are compared to their digital representations. Although only general purpose printers and materials were used, the steady advances in this emerging field allow that these economically priced prints can already prove helpful in the aforementioned use-cases.

Contents

Introduction

Vessels run through the entire human body and their visualizations are consulted to detect, track and treat both vascular and non-vascular diseases. *Arteries*, *arterioles*, *capillaries*, *venules* and *veins* are the five types of blood vessels, but only arteries and veins can be seen in a Computed Tomography (CT) or Magnetic Resonance Imaging (MRI) scan, due to their current spatial resolution of approximately 500μm per voxel, which is ten times the diameter of arterioles. Capillaries and venules are even smaller.

Aneurysms are a defect of the vessel's wall and occur mainly in arteries due to the higher blood pressure there. In the aorta, aneurysms are a special case and called *aortic dissections* (lat. aneurysma dissecans aortae). The aorta is lined with endothelial cells, which are part of the *tunica intima*, the first of three layers of arterywalls (also see Figure 1.1). The second layer is the *tunica media*, followed by the *tunica externa* or *adventitia*. The layers are separated by elastic membranes called *elastica interna* (between *tunica intima* and *tunica media*) and *elastica externa* (between *tunica media* and *tunica externa*) (compare [38]).

An aneurysm at the *aortic dissection* occurs through a tear in the *tunica intima*, whereby the blood flows between the *tunica intima* and *externa* bloating up a secondary, so called false, lumen. This lumen's size depends on the blood pressure and stability of the media, but can even exceed the size of the original (or true) lumen. The *tunica intima*'s tissue, which separates the true and false lumen, is called *intimal flap*. The dilation may even decrease or suppress blood flow to outgoing arteries. Depending on whether the *ascending aorta* is involved or not, *aortic dissections* are grouped in type A and B (see Figure 1.2). An *acute type A dissection* is the most dangerous one. Two percent of the concerned patients die per hour.

The visualizations of vessels are based on Computed Tomography Angiography (CTA) or Magnetic Resonance Angiography (MRA), where a contrast agent is used in combination with standard CT or MRI to increase the blood's visibility in generated images. The
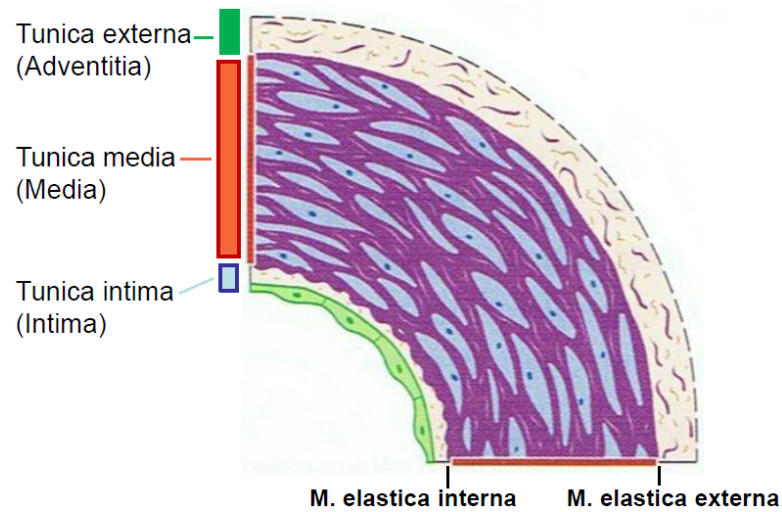
Figure 1.1: Structure of the aorta [16].

resulting data consists of slice images, over which the desired information is spread, and visualization techniques are needed to avoid looking at each slice one-by-one. As these visualizations also serve for operation planing, they have a crucial impact on the patient's health outcome.

There exist various methods to present vessels, each aimed for different pathologies, but as this thesis concentrates on *aortic dissections* only techniques suitable for detecting and analysing aneurysms are of interest. Visualization of the aorta's exterior is important to find the dissection's location, to determine its type and rate the severity. The aorta's interior is relevant to locate the tear, determine its length and find potential secondary tears.

In a Maximum Intensity Projection (MIP) from MRA data (as seen in Figure 1.3) the size, the true and the false lumen of an *aortic dissection* can be determined. The intimal flap can be seen as dark line between the true lumen and, due to less blood flow into the pathological volume, the less bright false lumen. But obviously, this visualization depends on the viewing angle and proportions of true and false lumina might be misleading due to superimpositions.

Vessels are tubular objects and thus hollow inside. To visualize the interior, geometric processing is necessary. A visualization that focuses on the interior of a vessel is Curved Planar Reformation (CPR) and its improvements Rotating CPR and Helical CPR [19; 20]. In Rotating CPR, the whole length of a vessel is re-sampled along its centerline and visualized through multiple images in different angles from the central axis [19]. Helical CPR goes one step further, by visualizing the whole interior in one image. Vascular abnormalities at any location, which have not been touched by the image plane of a Rotating CPR, appear in the image generated by this method [20]. The good representation of internal wall structure is on cost of spatial orientation,
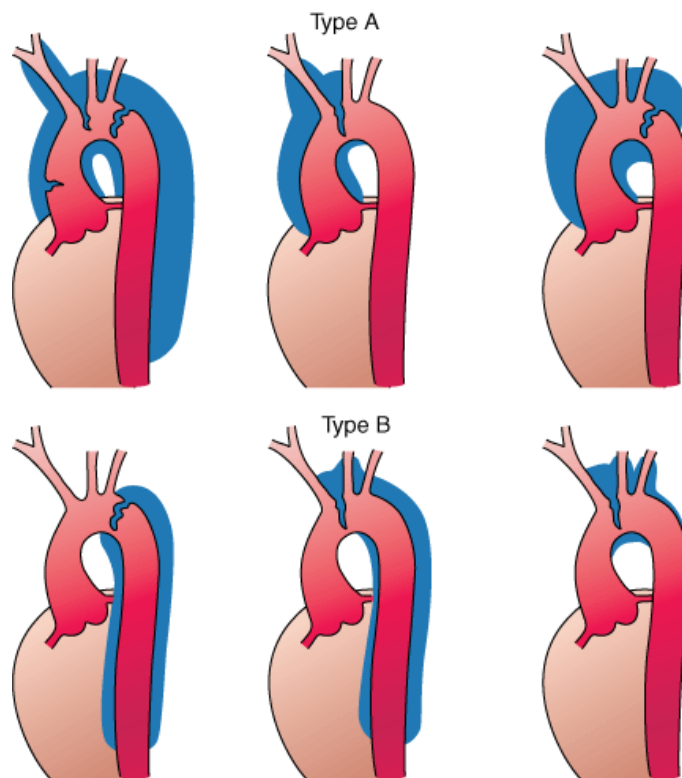
Type A

Type B

Figure 1.2: Stanford classification of *aortic dissections*. Type A involves the *ascending aorta* and possibly the *aortic arch* and *descending aorta* while Type B may only contain the latter two.

enhanced by the 180 degree rotation the *aortic arch* does after its origin from the *left ventricle*. Curvicircular Feature Aggregation (CFA) also offers vessel inspection by a single image [27]. Circular rays are cast around the centerline, and samples are generated along these rays. The samples of a ray are represented with methods such as MIP or Minimum Intensity Projection (MinIP). Because that single value contains information about the whole ray, displaying one half of the vessel is sufficient, as the other would have the exact same values. Instead another projection technique might be used as in Figure 1.4, with MIP and MinIP side-by-side. CFA is targeting *vessel stenosis* and occlusion, thus care should be taken when used for *aortic dissection*, as the vessel may no longer sustain its circular structure assumed by the rays cast around the centerline.

The current gold standard for vascular diagnosis is Digital Subtraction Angiography (DSA), which does not rely on tomographic data [27; 4; 17]. X-Ray images of the patient are taken before and after injecting a contrast agent and are then subtracted so the only difference, the dyed blood inside the vessels, is remaining. Thus, in simple terms an image
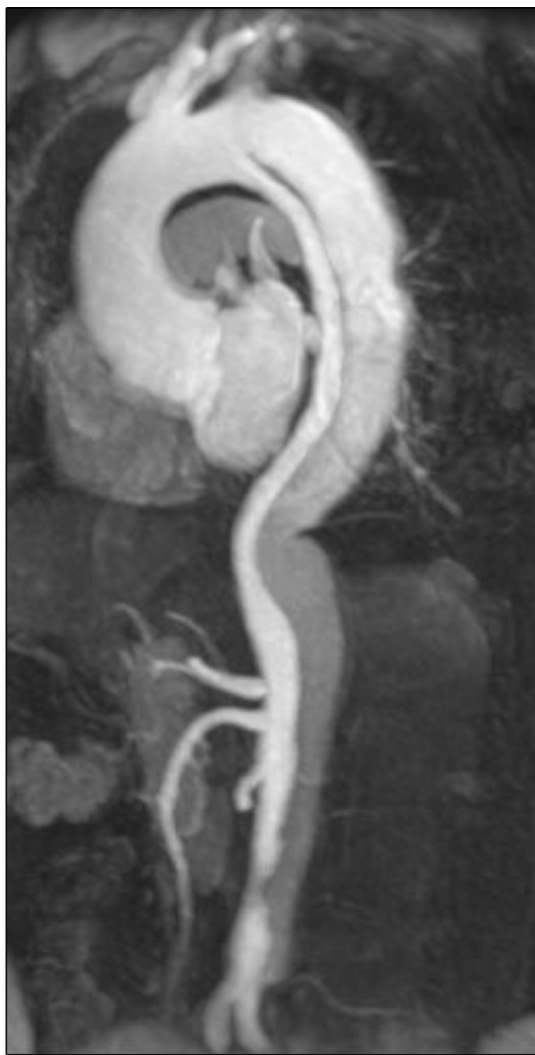
Figure 1.3: Image of a *type B aortic dissection* from MRA, displayed with a MIP [5].
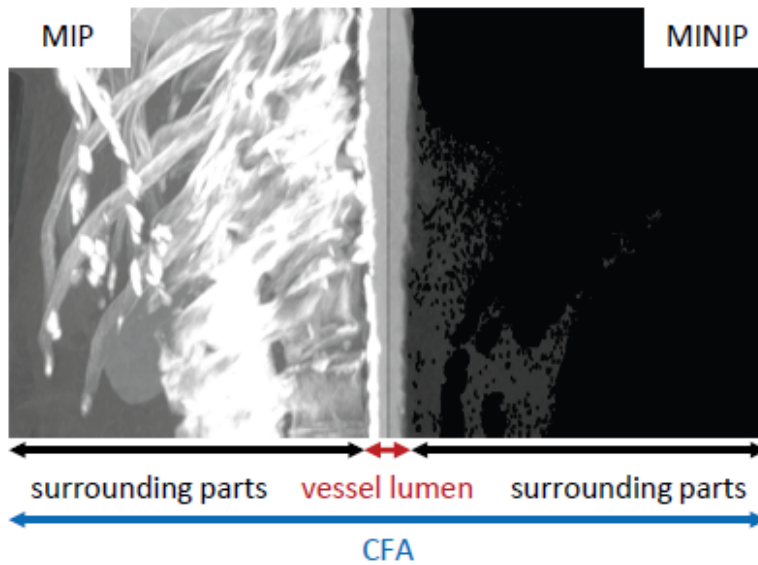
Figure 1.4: CFA of *abdominal aorta* with MIP and MinIP [27].

of the blood is taken. Extensions to 3-dimensional images are the already mentioned CTA and MRA.

As one can see, on the one hand 3D visualizations offer no look inside and navigating in the narrow tube is impractical. Methods to visualize lumen on the other hand, are either not targeted for aneurysms and their special shape, or are no longer as intuitive. Either way, the 3D structures are viewed on a 2D screen and an actual tangible model will always surpass an imagined one [41].

That is why a 3D print of the aorta is suggested in order to plan surgery. A tangible model of the pathology can be beneficial to plan and show surgical steps, rather than on a 2D screen. With separate printable true and false lumina of the aorta, one can intuitively check its course, see sections that are dissected and where a tear is in the wall.

First, points along the aorta have been taken individually, were stringed together and then converted in printable STereoLithography (STL) files. In the next step, the points were used to define a spline to set the course of a non-hollow cylinder with an arbitrary radius. To create a vessel-like hollow tube, the ability to set an arbitrary inner radius was added subsequently. Finally, real varying radii were used and applied along the tube. As a special feature, an extension to support vascular trees was added as well. Unfortunately, the segmentation of true and false lumina was not available at the time. However, it is expected that the delivered data is in the same format as used in the steps above. Hence, printing will be possible right away.

In the following section current uses of 3D printing in medicine are analysed, followed by methodology and report of implementation. Chapter 5 shows results of the work

done. Finally, the thesis ends with critical conclusion and thoughts on future work are discussed.

3D Printing in Medicine

To print 3D models, three dimensional base data is needed. In the medical domain, this is usually tomographic data obtained via CT or MRI, but ultrasound techniques (e.g. 3D echocardiography) can also be used to capture suitable data [47]. Once the desired volume data is segmented, it is converted into a file format known by 3D printers respectively their software. Most common formats are STL and Virtual Reality Modeling Language (VRML) [32]. For further information on these formats, please see Section 4.4.

2.1 Creation of 3D Models

Current 3D printers have a resolution of 100μm to 200μm with rather cheap general-purpose plastics such as polylactide (PLA) and polyethylene terephthalate (PETG), whereas CT scans have resolutions of about 500μm. High resolution scans may shrink voxels below 100μm, but by using better printers and other materials, prints with resolutions of just 10μm are also possible [1].

The model itself is printed in layers, why it is also referred to as additive manufacturing. Depending on the shape, support material may be needed to prevent parts of the model from falling down or tilting. The additional material is washed out with water or chemicals in a later stage of the printing process, and the final print will remain.

Another source of data are laser scans [40]. Most of today's hearing aids are 3D-printed from laser scans, speeding up the process of creating the final shell from more than a week to a single day [40]. As an example, Neuroth, an Austrian hearing-aid manufacturer, creates hearing protectors with 3D printers from digitized ear impressions [33].

Other fields of application for 3D prints in the medical domain include patient information, student education and surgical planing with hands-on training of which some examples from the literature are now discussed.
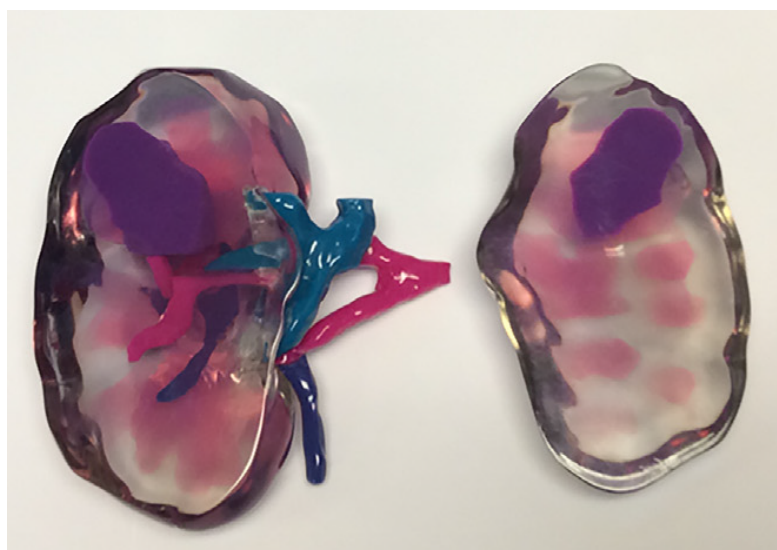
Figure 2.1: 3D-printed kidney model. *Renal medulla* is transparent, pink spots are the *renal cortex*, the purple spot is tumor tissue and the vessels are printed in red for the *main renal artery*, in blue for the *main renal vein* and in dark blue for the renal collecting system [45].

2.2 Models for Patient Communication

Patients diagnosed with renal malignancies often have lesions discovered incidentally through the necessary CT, potentially demanding additional surgery [41]. A common problem during the following doctor-patient encounter is to describe the pathology and required interventional actions on a 2D image [30]. The lack of patient's comprehension for the needed surgery may result in poor treatment choices by the patient and thus undesirable future outcomes [41; 30; 45]. Wake et al. printed kidney models with transparent *renal cortex* and then used combinations of cyan and magenta for the remaining structures as seen in Figure 2.1 [45]. Silberstein et al. used 3D-printed kidney models to improve the patient's comprehension of actual renal mass, tumor localization and size of malignant tissue [41]. The U.S. National Institutes of Health also predict usage of 3D models to show planed treatments and disease process [31].

2.3 Models for Surgical Planing and Hands-on Training

Not only the patients benefit from the physical model, but also physicians, radiologists and surgeons. They reported that touching aids perception of the anatomy and the models used for surgical planing provide guidance and serve as visual aid during the operation [12; 45].

Jardini et al. created a 3D skull model of a patient who suffered from a large cranial defect. That model was then used to design and to customize a titanium implant. Surgery time with this approach was around two hours, in contrast to three hours that such an operation would take if the implant is formulated manually. This reduces the anesthesia period, as well as the risk of infections [18].

Investigating whether 3D models could provide additional information to surgeons, paediatric cardiologist Matthew Bramlet started to print heart models. He immediately found another, commonly unseen, defect with the first model while also showing the other anatomy correctly [39; 29]. This changed the course of surgery and was not an isolated incident, which is why he started to create an online library[1] of congenital heart diseases [29].

In the branch of paediatrics where patients are in growth and are treated for (congenital) malformations, 3D-printed models are a tool to prepare for the challenging anatomy. Rose et al. created a 3D-printed model of temporal bone to train on before the actual surgery [36]. Another heart reprint was created at the University of Lousville. A 14-month old boy's heart had to be stopped during surgery as it suffered from a congenital defect. To take care of the organ but quickly perform surgery, the pre-operative look was "a game changer in planning to do surgery on a complex congenital heart defect" [10].

Yoo et al. created two different types of heart models with congenital disease: one that mirrors the heart's *endocardium* (and thus the inner surface), and one of the blood volume inside the vessels, *atria* and *ventricles* that provides "an excellent overview of the anatomy" [47]. Built with photopolymer resin, the material that resembles the modelled tissue most, hands-on surgical training is possible and expertise even in rare disease can be strengthened. With plenty of time, procedures can be trained, refined or even newly developed [47]. Hands-on surgical training on 3D prints also offers the possibility to test surgical instruments without risk for the patient [21].

At Montefiore Medical Center in New York City a 1-month old baby's jaw was printed. With the 3D model the undersized jaw that caused a breathing defect allowed the surgeons to explore the anatomy and figure out the right steps for the operation otherwise obtained via exploratory surgeries. As these surgeries are not feasible at such young age, the infant's condition would have been unchanged until years later without the model [13].

Bizzotto et al. created 3D-printed bone models with articular fractures, like *distal radius*, *tibial plateau* or *calcaneus fractures*. Gypsum-dust material was taken as it has similar structure to bone. The models were then used to preoperatively select and position plates and screws [7]. This pre-operative plate fitting is depicted very well in another work by Bizzotto et al. that focuses on *distal radius fractures* and can be seen in Figure 2.2 [8]. Intraoperatively the models supported spatial orientation [7; 8]. Furthermore, the piece of personalized medicine was very well received by the patients and increased understanding of their fracture [7].

---

[1]Heart models can be found at `http://3dprint.nih.gov/collections/heart-library`.
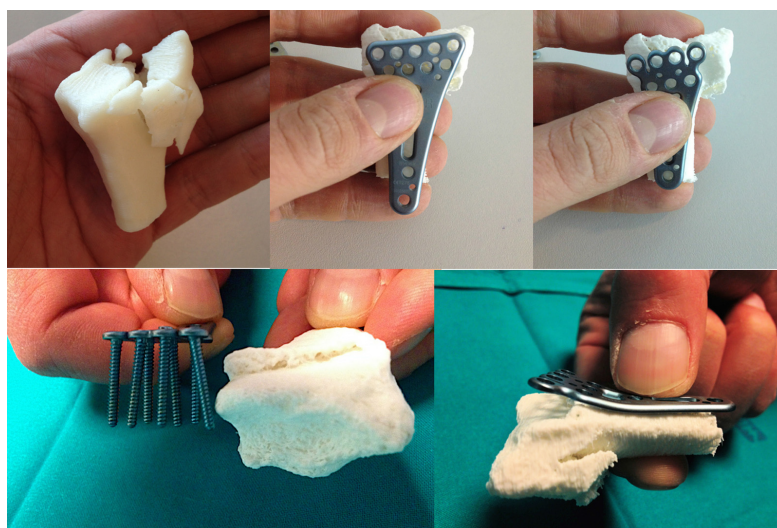
Figure 2.2: Preoperative selection and positioning of plates and screws for fixation of *distal radius fracture* [8].

Figure 2.3: 3D-printed upper limb replica [26].

2.4 Models for Student Education

Another use-case of 3D printing in medicine is the teaching of morphology with models instead of samples from classic pathological and anatomical collections. Even though these real samples are the superior source, they are not available for every pathology and have limited durability. Varieties of heart diseases can be collected, like Mattthew Bramlet does in the aforementioned online library, and then printed in desired numbers, size and views [47]. McMenamin et al. describes the disadvantages of current dissection-based teaching including ethical and cultural issues, but also financial ones. They produced several models, including negative space models of air or blood-filled cavities like *air sinuses* and *coronary vessels*. A upper limb replica from McMenamin et al. can be seen in Figure 2.3. Due to the lack of elasticity of these replicas and inability of students to perform clinical procedures, the author's view is that these 3D prints can not replace the traditional cadaver dissection, but augment it [9]. We can treat them rather as an alternative to plastinated specimens. The Monash University, to which McMenamin belongs, in cooperation with German anatomical model maker Erler-Zimmer GmbH now

sells a 3D-printed anatomy series[2] for use in medical schools [15].

2.5 Other Areas of 3D Printing in Medicine

In addition to human medicine, application in "veterinary anatomy teaching, zoological specimen reproduction" and "reproduction of rare museum specimens" is predicted [26].

On the outside of the body, Lin et al. made orthopedic casts with 3D printers. A patient-specific 3D-printed cast also features the perfect fit a plaster cast has, but with only a tenth of the weight and additional ventilation holes and an opening gap. These improvements significantly increase patients' satisfaction and also reduce irritations and infection risk beneath the cast [22].

2.6 Related Work

Mitsouras et al. give a great overview on 3D printing in medicine, showcasing many clinical applications of which some have already been discussed. Those with special similarity to the thesis' topic are now discussed separately. A *tracheabronchial tree*, with a shape similar to a vessel tree was 3D-printed with flexible material and used for preoperative *bronchoscopy* simulation [28].

Work of Markl et al. who created aortic replicas from MRA data is also featured. Of particular interest in this aorta model (see Figure 2.4) is the aneurysm in *right subclavian artery* and the branch-offs from the *aortic arch*, which can also be seen from the inside in Figure 2.4c. The blood pool was segmented from MRA data, which can be done rather easily due to enhancement via the contrast agent [25]. As the blood pool only gives information about the inner surface of the aorta, an artificial outer surface had to be added to be 3D-printable [25; 28]. Another approach would be to convert the blood pool and surrounding tissue to STL format and then subtract the structures to hollow out vessels [28].

Håkansson et al. investigated a *thoracic* and a *abdominal aneurysm* using a life-size silicone aorta model. Initially the inner volume was segmented from CTA data, with calcified plaque removed so the real remaining inner diameter is represented. The inner volume was than printed in three parts to fit into the printer. After glueing the parts together, the printed plaster model was coated with silicone. The final result can be seen in Figure 2.5. The silicone coating was repeated up to a thickness of roughly 3mm. Therefore, the model's surface does not resemble the vessel's hull but it's inner surface, similar to the approach of Markl et al. described above.

With lost-wax casting[3] a comparable technique was used by O'Reilly et al. to create models of *femoral arteries*. With a soluble powder, cores of blood vessels were printed.

---

[2]http://www.3danatomyseries.com/
[3]https://en.wikipedia.org/wiki/Lost-wax_casting
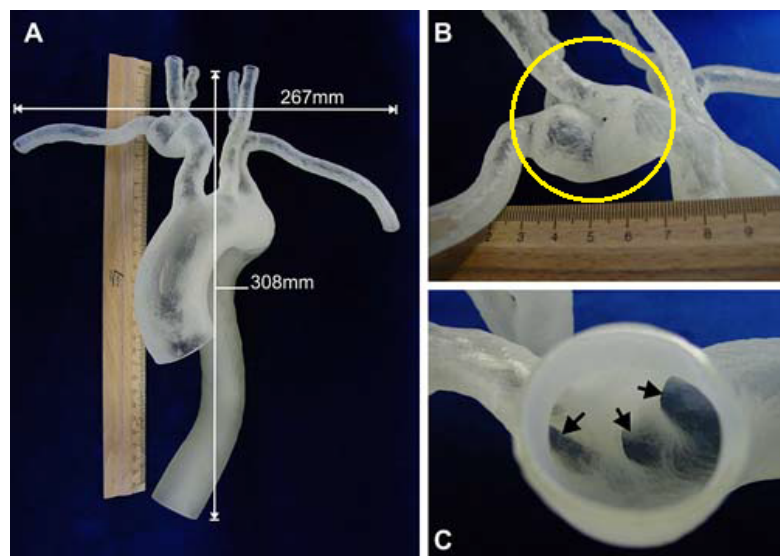
Figure 2.4: A) 3D-printed arch of the aorta; B) Aneurysm (yellow circle) in *right subclavian artery*; C) Look inside aorta with branching off vessels (arrows) viewed upwards from *aortic valve* [25].
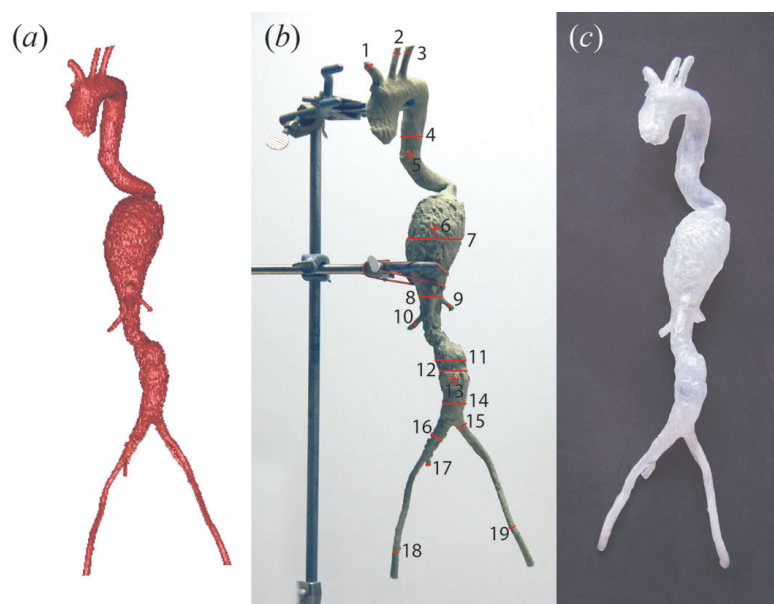
Figure 2.5: (a) 3D CAD model; (b) 3D-printed and assembled model; (c) Final silicone model [14].

These cores were first coated with magnesium sulfate and afterwards with silicone rubber. Once the coating had cured, the core was flushed out resulting in a hollow vessel replica. These vessels were then used to learn arterial puncture techniques guided by ultrasound. For realistic ultrasound images the vessels were perfused, placed besides 3D-printed bones and covered with gel wax as tissue [35].

Biglino et al. used a rubber-like material to print vascular models for in-vitro simulation [28]. By varying the wall thickness, distensibility similar to real arteries could be achieved and an *aortic arch* model was produced. It withstood the usually occurring pressures in a mock-up circulatory loop [6]. The same material was used by Kurenov et al. to create models of *pulmonary arteries* from CT and CTA data. With the models' help, the complicated anatomy could be intuitively studied and measurements for catheter design were taken [21].

To the best of the author's knowledge this is the first work on printing 3D models of *aortic dissections*.

Methodology

Vessel trees serve as input for the developed algorithms and produced models. Three methods have been developed to create 3D-printable models. Starting with simple coordinate data from points along the vessel's centerline, these were just converted one-to-one to see the vessel's course (see Section 3.1.1). A more appropriate method for printing is to create a spline along the centerline and assign either arbitrary wall thickness and inner diameter (see Section 3.1.2) or use real diameters if possible (see Section 3.1.3). Those two approaches were combined to convert a whole vessel tree for 3D printing (see Section 3.1.4).

The VISICIAN framework prepared to deliver meshes of true and false lumina in vtkPolyData format. As this is format is also accepted by the Visualization ToolKit (VTK) mehtods in use for STL printing, it is expected that printing of segmented data is possible without further adaptations.

3.1 Conversion Methods

All methods target on conversion from 3-dimensional coordinate data to polygonal meshes. At the end of each method, the resulting mesh was processed with VTK's vtkTriangleFilter[1]. This filter iterates over all polygons and replaces the ones with more than three edges via triangulation. The vtkSTLWriter[2] finally writes the triangles into a 3D-printable STL-file (see Section 4.4).

3.1.1 Centerline Point Conversion

With this simple method, conversion of 3D medical data to STL format was tested. With the bounds of the vessel's centerline points, a discrete volume grid was created

---

[1]http://www.vtk.org/doc/nightly/html/classvtkTriangleFilter.html
[2]http://www.vtk.org/doc/nightly/html/classvtkSTLWriter.html

and initialized with zero data values. Voxels inside the vessel tree were set to 255. The resulting mask is converted into polygons with Marching Cubes algorithm provided by VTK[3]. The Marching Cubes algorithm repeatedly reads cubes of 8 points and creates a triangle mesh that captures the isosurface inside each such cube [23]. The mesh is then processed as already described in Section 3.1.

3.1.2 Fixed-Diameter Tube Conversion

With vtkParametricSpline[4] a cardinal spline was defined along the centerline's points representing the vessel's course. To create a continuous vessel wall, this spline was tessellated with vtkParametricFunctionSource[5] that provides data to the vtkTubeFilter[6].

Unfortunately, this filter does only support creation of a tube with triangle strips around the spline's line normals. These triangle strips have zero thickness and thus printing is not possible, unless the tube is capped and thus filled. A capped tube however would be filled completely during printing making it undesirable.

Listing 3.1: vtkThickTubeFilter

```
Create tube with given inner radius
Create tube with given outer radius
Add inner tube polygons to mesh
Add outer tube polygons to mesh

numSides =  number of sides of a tube
numPoints =  number of points of a tube

while k < numSides; with point pi[k] of inner and po[k] of outer tube
{
    Create triangle: pi[k], pi[k+1], po[k]
    Create triangle: pi[k], po[k+1], po[k]

    //numPoints-numSides = index offset for other end
    Create triangle: pi[numPoints-numSides + k],
                     pi[numPoints-numSides + k + 1],
                     po[numPoints-numSides + k]
    Create triangle: pi[numPoints-numSides + k],
                     po[numPoints-numSides + k + 1],
                     po[numPoints-numSides + k]

    Add all triangles to mesh
    k++
}
```

To create a tube with some inner diameter and user-defined wall thickness, the third party library vtkKinship is used [44]. It contains the vtkThickTubeFilter that has methods to

---

[3]http://www.vtk.org/doc/nightly/html/classvtkMarchingCubes.html
[4]http://www.vtk.org/doc/nightly/html/classvtkParametricSpline.html
[5]http://www.vtk.org/doc/nightly/html/classvtkParametricFunctionSource.html
[6]http://www.vtk.org/doc/nightly/html/classvtkTubeFilter.html
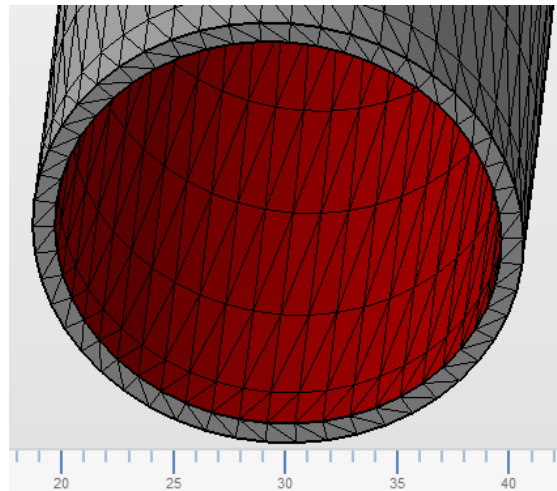
Figure 3.1: A fixed-diameter tube with 50 sides and 1mm wall thickness. Faces of the outer and inner wall are oriented in the same direction, causing a mesh problem after stitching them together. The misoriented faces inside the vessel are coloured red.

set both inner and outer radius of the tube. To connect the two tubes, the points on their respective ends are connected with additional triangles as described in Listing 3.1. The tubes' circular shape is approximated by a polygon. The number of the polygon's sides can by be defined via the user interface.

The vtkThickTubeFilter outputs vtkPolyData, and the stored polygons are converted to triangles and printed as described in Section 3.1. However, the faces of the inner wall had to be reorientated to create a proper mesh. Netfabb highlights misoriented faces in red, allowing easy identification (see Figure 3.1) [3]. Correction was done using vtkPolyDataNormals[7] filter, which can reorder polygons for consistent orientation.

3.1.3 Varying-Diameter Tube

The approach of Section 3.1.2 was improved by varying the tube's radii to match the real inner vessel radius provided in the tree data.

To create a printable volume, wall thickness was assigned outwards the vessel lumen. This preserves the inner shape of the vasculature and makes it visible on the outer surface as well. Because changing radii along the tube is not supported by the library's vtkThickTubeFilter, the used algorithm was enhanced to cover this use-case. Radii values are added to the spline data and the tube creating algorithm is set to vary the tube's radius by the given values. The resulting disconnected inner and outer wall of the tube are connected on their respective ends and the polygons are reorientated as described in Section 3.1.2.

---

[7]http://www.vtk.org/doc/nightly/html/classvtkPolyDataNormals.html
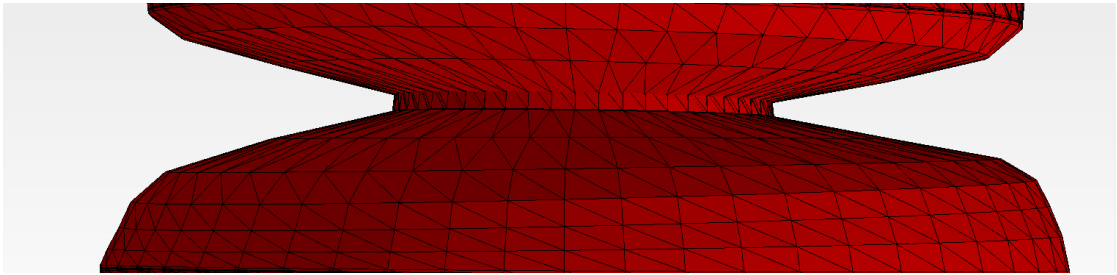
Figure 3.2: Radii variation of the generated tube. From top to bottom, the tube starts with a radius of 12mm, is first decreasing to 11.0mm, then 8.0mm and finally 4.6mm. Afterwards the radius shortly stays constant and then increases rapdily to 8.3mm, then 11.4mm, and then slowly to 12.4mm, 12.8mm, 13.2mm and finally 13.4mm.

While the available radii are discrete values at certain points, the tube's surface is piecewise linear between tessellant points and the radii get interpolated between these. To make this interpolation as smooth as possible, the number of tessellant points is set to the number of points in the vessel tree's path so that the applied radii coincide with the radii specified in EXtensible Markup Language (XML). Usage of radii at tube segment corners can be seen in Figure 3.2.

3.1.4   Vessel Tree

To create a vessel tree, the paths of it (see Section 4.1) were converted according to the method, described in Section 3.1.3 and the resulting polygon meshes were then combined with vtkAppendPolyData[8] algorithm.

At bifurcations, this combination results in occlusion of each vessel lumen by the wall of another path's tube heading in another direction. This problem is illustrated in Figure 6.1. Multiple approaches to prevent or remove vessel wall parts inside the lumen of another vessel have been examined, but none has proved viable, either because of complexity or by its results (also see Chapter 6).

---

[8]http://www.vtk.org/doc/nightly/html/classvtkAppendPolyData.html

Implementation

The code of this project was written in `C++` and embedded into the VISICIAN Framework. The user interface was created with `Qt5` [42]. XML data was processed with the TinyXML-2 library [43]. All conversion methods described in Section 3.1 are based on VTK [37].

4.1   Input Data: Vessel Trees

The input is tree-like structured vessel data, in two different formats. The first encoded in JavaScript Object Notation (JSON) used by the VISICIAN framework, where this project is embedded, and the second as XML used by AngioVis[1]. Despite some differences between these formats, the represented data is the same.

The vessels are described by 3D points, creating it's centerline with `x`, `y`, `z` coordinates and `r1` and `r2` as inner and outer radius. Points are combined into vessel segments, and multiple segments form a path. More precisely, segments are the vessel parts between bifurcations in the vessel tree, while paths connect these segments as seen in Figure 4.1. These paths form the described vessel tree.

Only one dataset in JSON format was available. It contains coordinates of points along the *abdominal aorta*, but without vessel radii. This JSON data could be read by the existing VISICIAN framework tools and was therefore used as first dataset. In XML format eight vessel trees with arteries of abdominal region and lower extremities have been used. These datasets also had inner radius data stored for each vessel tree point.

The XML structure of Figure 4.1 is exemplarily shown in Listing A.1. Attributes and nested structure are alike in JSON and thus not shown separately. Listing 4.1 shows how the XML files are parsed.

---

[1] `http://www.angiovis.org/`
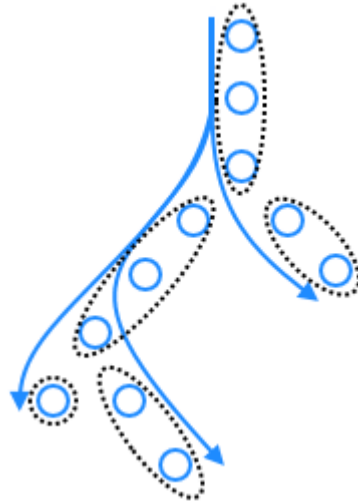
Figure 4.1: Representation of vessel tree elements. The blue circles represent the points along the vessel's centerline. The black doted ellipses group them into segments. The blue lines represent paths along segments.

Listing 4.1: Parse VesselTree XML

```
Create empty vessel tree

for each segment inside segments element
{
    Read segment id and Create segment
    for each point inside segment
    {
        Read coordinates and radius
        Add point to segment
    }
    Add segment to vessel tree
}

for each path inside paths element
{
    Create path
    for each segment inside path
    {
        Read segment from vessel tree by id
        Add segment to path
    }
    Add path to vessel tree
}
```

4.2 User Interface

The user interface is embedded as additional tab in the VISICIAN application. It was designed with `Qt 5.7` using the Designer tool, which generates a XML-coded UI-file. As seen in Figure 4.2, the user can select between different available input sources. Depending on the source, conversion methods described in Section 3.1 are available. The user can choose between segmented data, a vessel tree from the currently open VISICIAN session and an arbitrary XML-encoded vessel tree, loaded from the file system.

Segmented data offers no further options and would be converted as is. As soon as segmentation data is available in the application, the option becomes activated automatically and conversion to STL is possible without further adaptations.

The vessel tree from the current VISICIAN session does not feature radii information, which is why the option for varying diameters is not available. Instead the user can select between point conversion and conversion to a fixed-diameter tube. For point conversion, the number of voxel neighbours can be selected (see Figure 4.2a). A neighbourhood of 0, 6, 18 and 26 points can be chosen. For fixed-diameter tube conversion, the user is able to define inner diameter, wall thickness and the number of sides the tube should have (see Figure 4.2b).

The imported vessel tree has radii information and conversion method for varying tube diameters is selected (see Figure 4.2c). Vessel tree files also contain an outer radius for each point, but in the used data sets, the outer radius was always identical to the inner radius. Therefore the users can choose a wall thickness themselves. The tube's number of sides can also be changed.

4.3 Conversion

Apart from reading the XML-files, all steps in the conversion process were carried out with VTK methods (see Section 3.1) [37].

The spline is defined along all points of a path from the vessel tree, even though that causes segments, which belong to multiple paths, to be converted more than once. This step was necessary because tree segments do not perfectly match. They can intersect or be split from each other. Additionally, the radius of one segment's end does not necessarily match the radius of the next segment's beginning. Converting the vessel tree segment-wise thus causes several problems as seen in Figure 4.3, which is why always complete paths are used for tube creation instead of connecting them by further processing. This was a decision with regard to the soon available segmented data that can be converted voxel-wise.

Additionally, the subdivisions of the parametric spline had to be set for the varying diameter use-case (see Section 3.1.3). There are only as many radii as there are points, so the resolution in parametric direction `U` had to be set to number of points minus one.
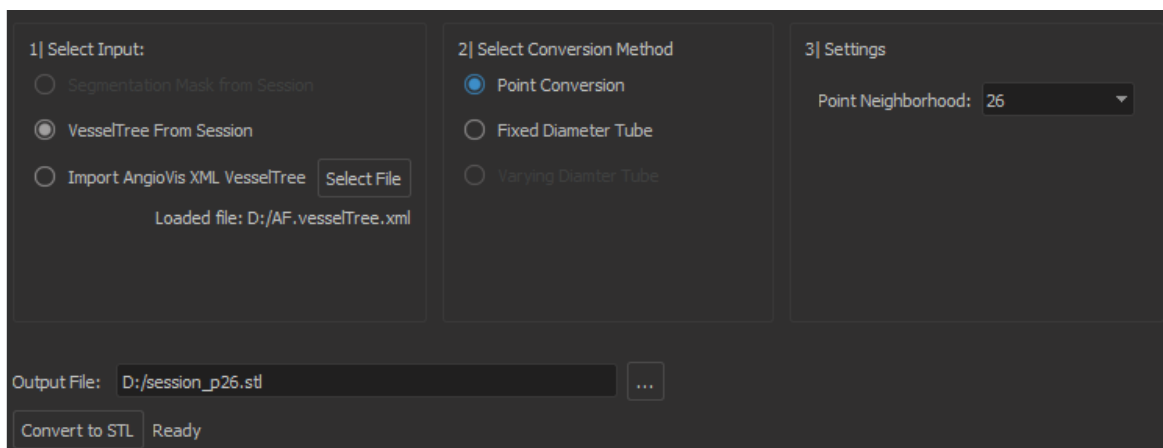
(a) Settings to convert the points of the vessel tree and its neighbours.
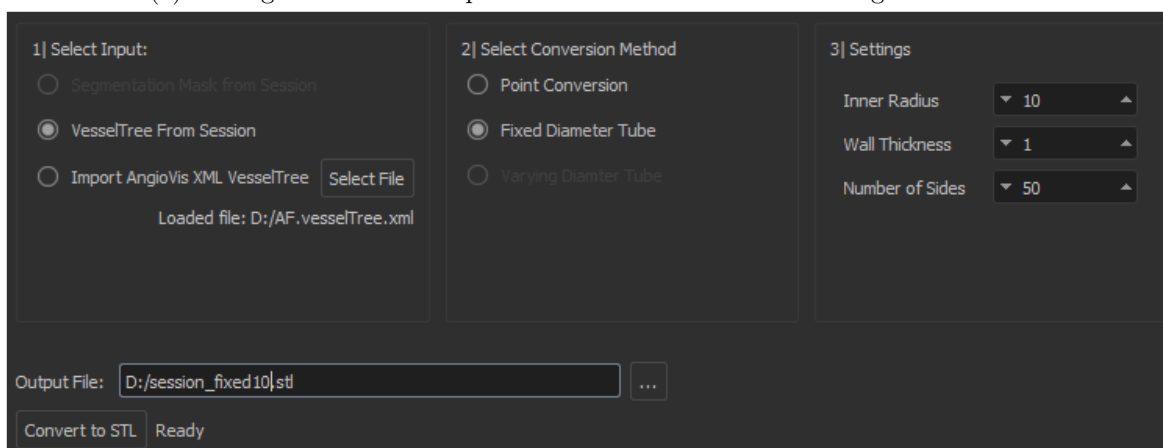
(b) Settings to convert the vessel tree to tubes with fixed diamter.
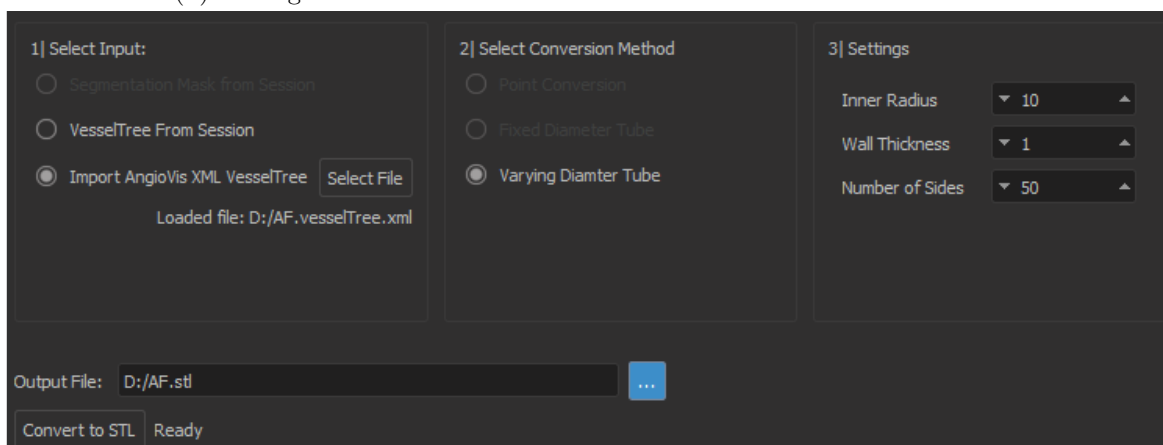
(c) Settings to convert the vessel tree to tubes with varying diameter.

Figure 4.2: Different UI settings dependent on the input.
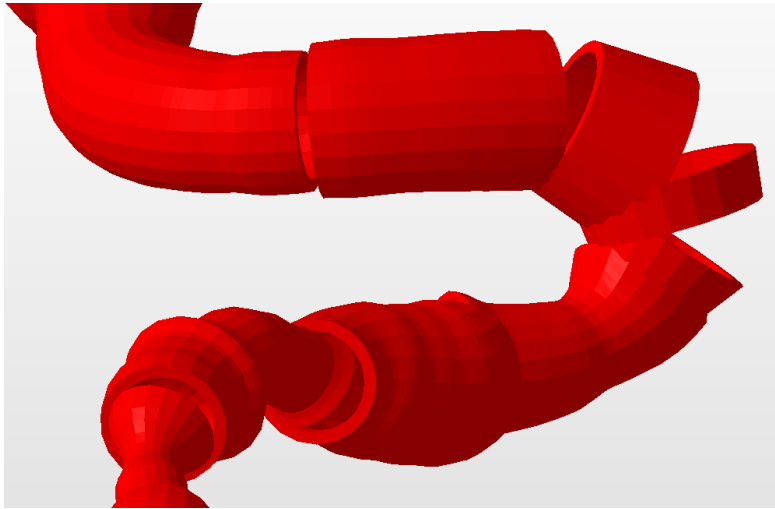
Figure 4.3: A vessel tree created segment-wise. Please, note that the segments at bendings do not connect. Straight sections of the vessel tree also have gaps due to the subtle orientation and radius differences.

As we have one more tessellant point compared to the number of points provided, it equals to the number of radii available.

Conversion of AngioVis vessel trees into a polygon mesh takes approximately ten seconds and is then written to the file system as STL-file. The conversion of paths is done sequentially in one thread.

4.4 Output Data

STL files describe the surface of an object to be printed with triangles and support only a single colour [2]. Two distinct representations, namely ASCII and binary, can be used. While with ASCII, a human readable text file is created, binary representation leads to a lower file size and thus also a shorter runtime of the algorithm, as less data needs to be written. VTK starts an ASCII STL file with `solid ascii` and ends it with `endsolid`. In between, each polygon is described like in Listing 4.2.

Listing 4.2: ASCII STL triangle representation.

```
facet normal n1 n2 n3
    outer loop
        vertex v1x v1y v1z
        vertex v2x v2y v2z
        vertex v3x v3y v3z
    endloop
endfacet
```

VRML supports multiple colours and stores vertices and edges of polygons in a text file like STL [46]. Another format is the Additive Manufacturing File Format (AMF), a rather new XML-based format that also has colour support [32].

Each of these formats needs to be converted into a printer-specific G-Code [32]. Among other things, the G-Code has instructions where to move and when to start or stop printing [24].

The resulting STL-files in ASCII format from AngioVis vessel trees have a file size from 300 to 400 Megabytes and contained from 1.6 to 2.25 million triangles for tubes with 50 sides. By changing STL encoding from ASCII to binary, the file size was lowered to approximately 50 Megabytes (also see Chapter 5).

All generated files were verified for 3D-printing geometrical constraints with MeshLab and Autodesk Netfabb [11; 3]. Both show information about the model and MeshLab has a variety of manual manipulation and repairing options. Netfabb also shows the mesh's correctness and has automatic repair options and was used to scale the models down to fit into common printers.

CHAPTER 5

Results

Five datasets were chosen for 3D printing in evaluation purposes. The first dataset contained the thoracic and abdominal section of the aorta and has been converted with a fixed radius of 10mm and wall thickness of 1mm. The resulting 3D-printable model consists of 10200 triangles, measures 348mm along the longitudinal axis and has file size of just 500 Kilobytes.

To reduce manufacturing costs, the model was scaled down to a height of 200mm with Netfabb. By cutting the model into two parts, a flat bearing surface was created that reduced the amount of required support material. These two parts were printed with a `Makergear M2` and PLA at 200μm layer height and can be seen in Figure 5.2c.

Print quality of this first model is good for visual assessment and the circular shape is very well approximated by the 50 sides. The exterior was printed without any irregularities and is on par with the computer representation (compare Figure 5.2).

When held against light, the spline's subdivisions can be seen on this model (see Figure 5.1b). The inner wall surface suffers from some sticking out filament pieces and a less smooth surface at the topmost area of each shell, compared to sidewise walls (see Figure 5.1a). At these most overhanging areas, support structure is necessary during printing and deformations caused by the material's cooling are more likely.

(a) Surface of the tube's inner shell. While the surface is very smooth at the sides of the tube, it gets rougher towards the middle where support material was needed.
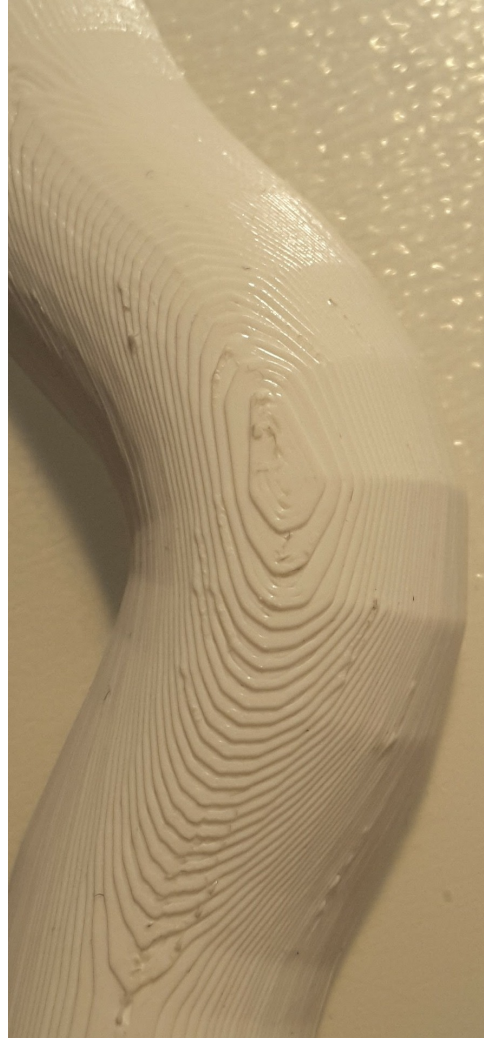
(b) Spline subdivisions from a printed model can be seen at stronger curves. The layered structure is also highly visible.

Figure 5.1: Close-ups of printed tube's inner and outer surface.
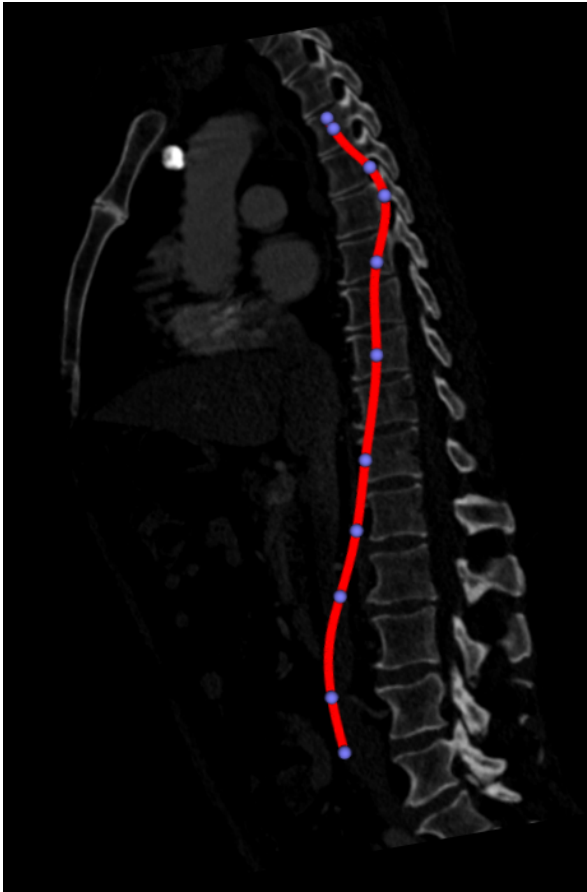
(a) The tube's path in VISICIAN.
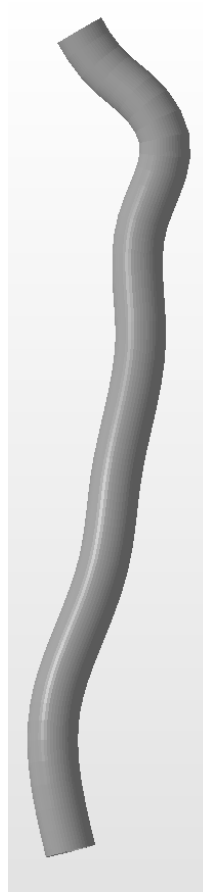
(b) The tube's STL model displayed in Netfabb.

(c) The 3D-printed tube with fixed-diameter.

Figure 5.2: The fixed-diameter tube print in comparison to digital renderings. Aside from subtle camera angle differences, the vessel's course is preserved after converting to STL (b) and printing (c).
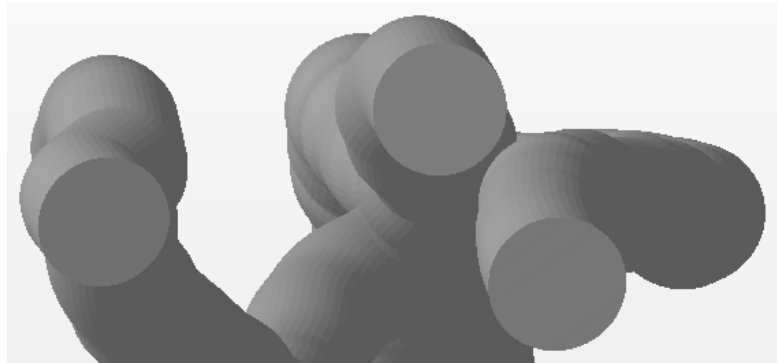
Figure 5.3: Vessel tree with filled branches.

All other tested 3D-prints stem from vessel tree data with varying radii. The trees originate in the *abdominal aorta* and descend into the *femoral arteries* and then further into the *anterior* and *posterior tibial artery* and the *peroneal artery.*

The 3D model of the first tree dataset consists of 1.05 million triangles, has a height of 1338mm and a file size of 51 Megabytes. The model was scaled down to a height of 200mm as well. Due to the enormous height, the scaled-down vessel walls became to thin to print. Even after increasing wall thickness, the vessel walls were unprintable. Therefore, the vessel trees had to be printed with filled tubes (see Figure 5.3).

The second tree has a height of 1201mm, consists of 802.076 triangles and has a file size of 39 Megabytes. The third dataset has a height of 1196mm, consist of 998.276 triangles and its file size is 49 Megabytes. The last is 1137mm high, its surface consists of 1.13 million triangles, which also leads to the highest file size of 55 Megabytes. All three suffered from the same problems as the first model after scaling-down and were thus printed filled as well. The resulting models can be seen in comparison to the renderings in AngioVis and Netfabb in Figures 5.6 to 5.9.

A `Original Prusa i3 MK2` printer was used to print them in a layer height of 150μm with red `HD Glass`. Due to their varying radii and unsteadier course, the layers of these prints are not as clearly visible as in the case of the fixed-diameter print (see Figure 5.1b). Even though the models have been shrunk to just $\frac{1}{6}$ of their original size, details are surprisingly well preserved (compare Figures 5.4 and 5.5). This is promising for bigger or life-size prints of particular vessel tree sections that are of interest for the current examination.

For such scaled-down objects, visualization on the computer remains superior as the triangle representation is independent of the object's physical size. This is also reflected by the file size, which remained unchanged after the models were scaled down to their printed size.
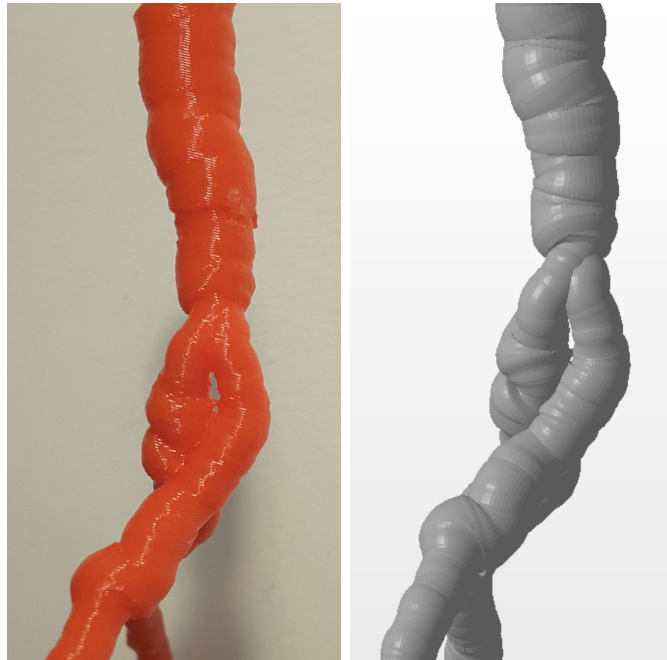
Figure 5.4: A tiny gap between the two vessel branches can be seen right after their origin in Netfabb (right) and at the printed model (left).
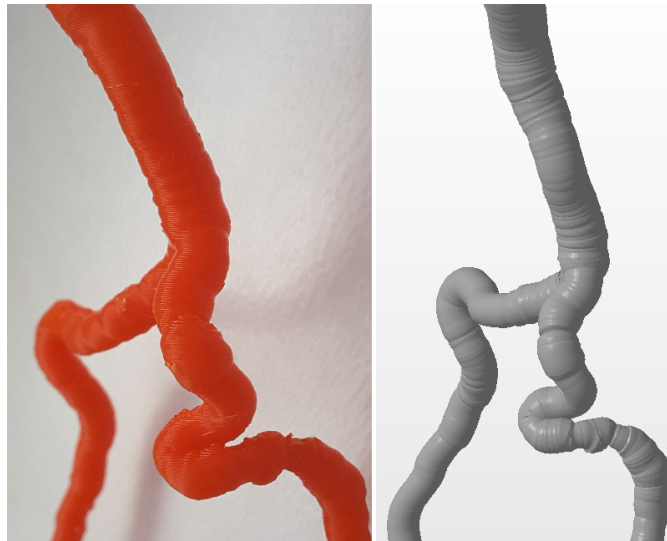
Figure 5.5: The turnaround of the branch and its varying radius can be observed on the scaled-down print (left) just as in Netfabb (right).

(a) AngioVis overview of first vessel tree.

(b) Vessel tree in Angio-Vis reformation window.

(c) The model displayed in Netfabb.

(d) Final 3D print of the model.
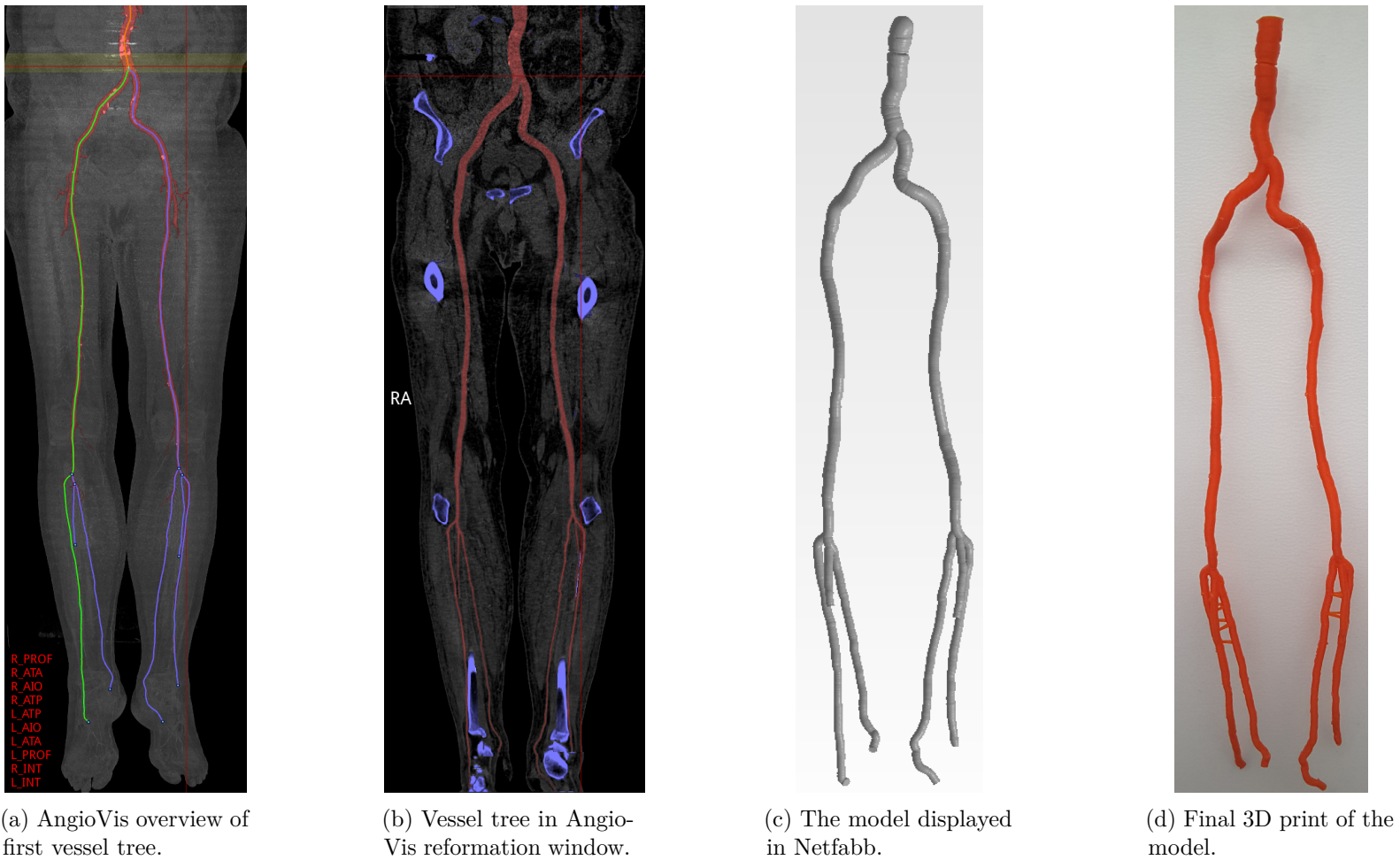
Figure 5.6: First vessel tree dataset in comparison. Between AngioVis (a,b) and 3D model (d) the similiar bending of the *left iliac artery*, *left peroneal artery* and *right peroneal artery* can be observed.
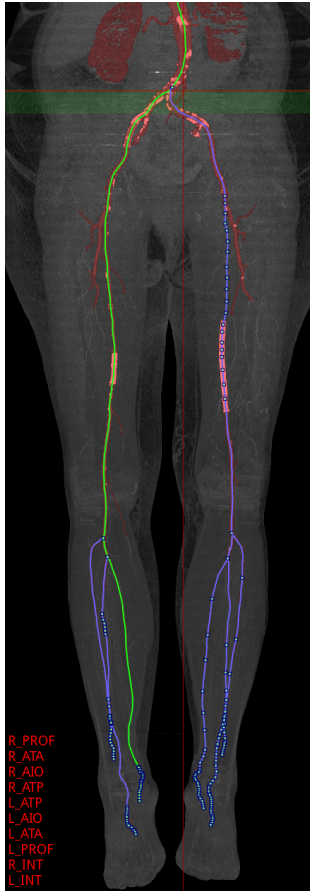
(a) AngioVis overview of second vessel tree.

(b) Vessel tree in Angio-Vis reformation window.
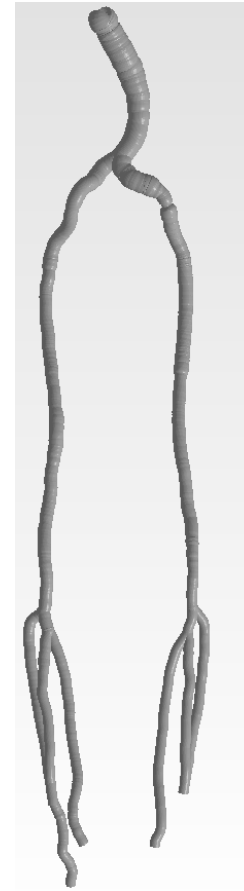
(c) The model displayed in Netfabb.

(d) Final 3D print of the model.

Figure 5.7: Second vessel tree data set in comparison. Occlusion of *right iliac artery* can be seen in Angiovis reformation window (b) and is reflected by the decreased radius in the printed model (d).

(a) AngioVis overview of third vessel tree.

(b) Vessel tree in Angio-Vis reformation window.

(c) The model displayed in Netfabb.

(d) Final 3D print of the model.
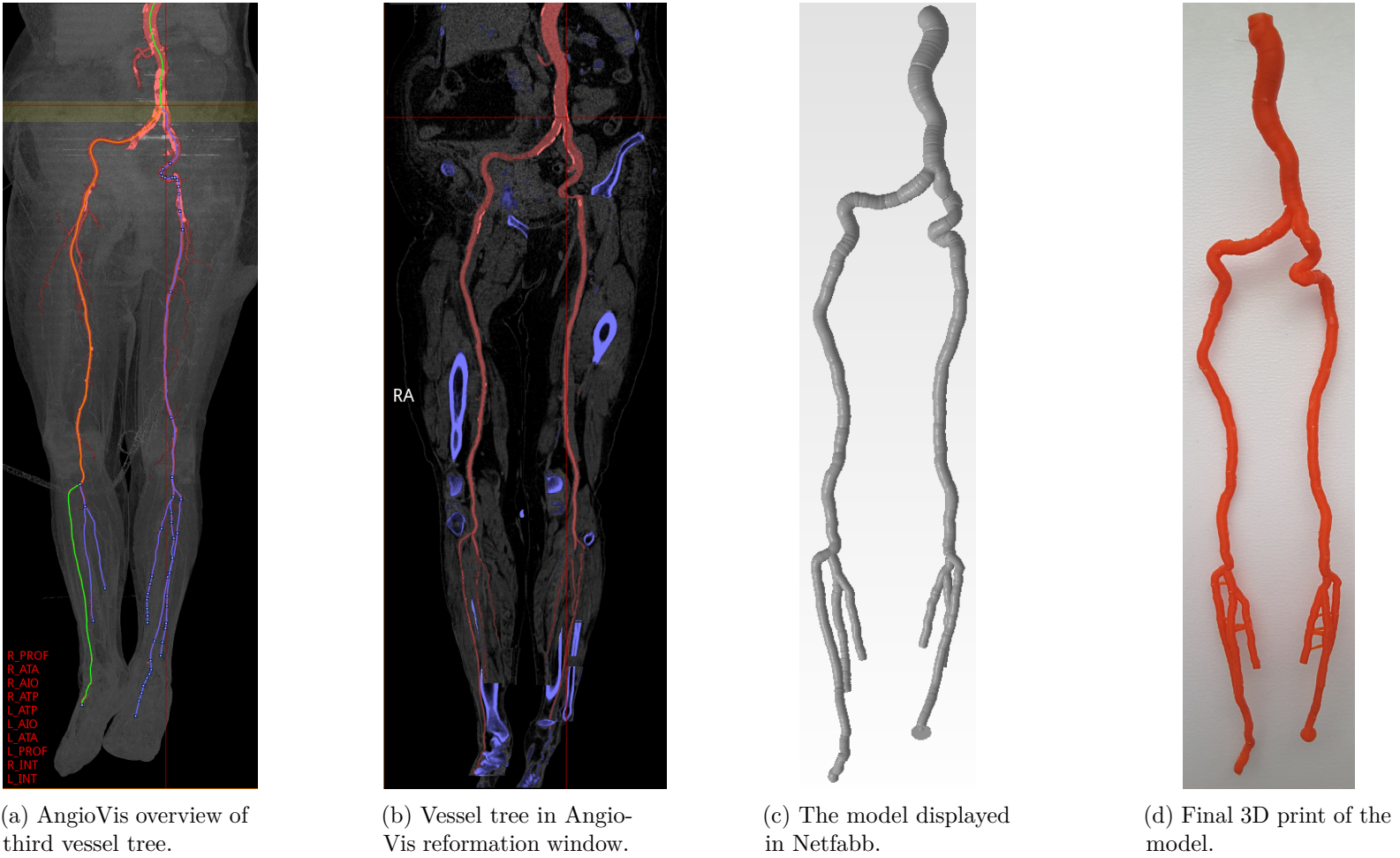
Figure 5.8: Third vessel tree dataset in comparison. The characteristic bending of the arteries in the groin can be observed in digital representations (a-c) as well as the 3D print (d).

(a) AngioVis overview of fourth vessel tree.

(b) Vessel tree in Angio-Vis reformation window.
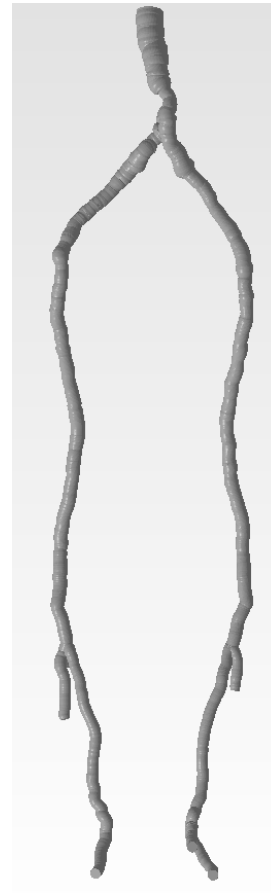
(c) The model displayed in Netfabb. The filled tubes can be seen at the end of the *posterior tibial artery* at the bottom.

(d) Final 3D print of the model.

Figure 5.9: Fourth vessel tree dataset in comparison. The course discrepancy of the *posterior tibial artery* between Netfabb (c) and the 3D print (d) stem from camera angle differences. Apart from that course and radii changes are well transferred to the 3D print.

CHAPTER 6

Conclusion and Future Work

With points along the vessel's centerline, tubes with fixed and varying diameters have been created and were combined together to print whole trees of vessels. For evaluation purposes, five prints were created: one of a tube with fixed-diameter and four of vessel trees with varying diameter. Changes of direction and variations of the radius and even small characteristics visibly correspond to the actual computer renderings.

An open problem is that the walls of the single tubes created from the vessel tree's paths occlude each other at branchings (see Figure 6.1 and Section 3.1.4). We were unable to solve this issue currently, as it requires significant amount of geometrical operations to detect such occlusions.
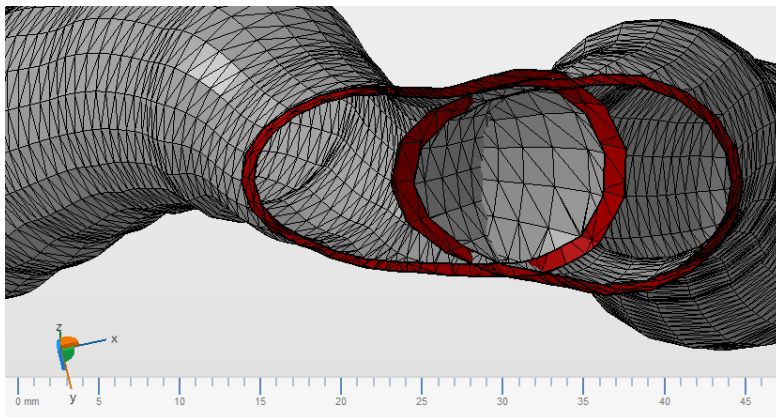
Figure 6.1: Overlap of vessel tree walls in distal direction. The vessel tree is cut at a bifurcation. The occluding walls remaining inside the lumen can be seen in the middle (between 24mm to 37mm on the scale). The wall shapes appears elliptical because the cut was not done normal to the splines.

Figure 6.2: Close-up of 3D print from a segmented aorta. The uneven surface leads to a better perceived quality, even though printer and printing parameters were the same as for the fixed-diameter print (compare with Figure 5.1 and 5.2).

All prints have been scaled-down to be fabricable by common 3D printers. This lead to inexpensive models on the one hand, but introduced problems with thin walls on the other hand. They had to be thickened which distorts the result on smaller vessels where their walls became thicker than the vessel themselves.

The models discussed in Chapter 2 all cost several hundred dollars in fabrication. The costs for all our evaluation prints amount to about 50 euro. Even with this significant difference, the created models offer good details and convince even more when the surface is less straight and geometrical. The stepped surface from the additive manufacturing method fades in background the more a model's course and radius varies (compare Figure 6.2 with Figure 5.1).

How prints with segmented data could look like can be seen in Figure 6.3. The aorta model with a *saccular aneurysm* by Nevit Dilmen [34] was scaled down to 80% of its original size, truncated and split. With a `Makergear M2`, it was printed with PETG and a 200μm layer height, just like the model with fixed-diameter.

Besides the use of segmented data, there are additional features suitable for future work. Two prints presented in this thesis were cut in Netfabb with a straight plane to ease and accelerate the printing process. The cutting plane was not easy to orient such that the parts became somewhat equally sized. VTK's tube algorithm allows the

Figure 6.3: 3D print of a segmented aorta with *saccular aortic aneurysm*.

omission of particular sides of the tube. This feature could be used to have the tube automatically split along a defined surface that takes its course like the tube. Another possible application of this feature would be to cut out certain sides and thus create a viewing window offering a look inside the tube.

Appendix

Listing A.1: XML VesselTree example of Figure 4.1

```xml
<!DOCTYPE AVPvesseltree>
<vesseltree>
    <segments count="11">
        <segment type="centered" id="1">
            <points count="3">
                <p>
                    <x>100</x>
                    <y>100</y>
                    <z>1</z>
                    <r1>3</r1>
                    <r2>4</r2>
                </p>
                <p>
                    <x>100</x>
                    <y>90</y>
                    <z>1</z>
                    <r1>3</r1>
                    <r2>4</r2>
                </p>
                <p>
                    <x>100</x>
                    <y>80</y>
                    <z>1</z>
                    <r1>3</r1>
                    <r2>4</r2>
                </p>
```

```xml
                    </points>
                <segment type="centered" id="2">
                    <points count="3">
                    <p>
                            <x>90</x>
                            <y>70</y>
                            <z>1</z>
                            <r1>3</r1>
                            <r2>4</r2>
                        </p>
                        <p>
                            <x>80</x>
                            <y>60</y>
                            <z>1</z>
                            <r1>3</r1>
                            <r2>4</r2>
                        </p>
                        <p>
                            <x>70</x>
                            <y>50</y>
                            <z>1</z>
                            <r1>3</r1>
                            <r2>4</r2>
                        </p>
                    </points>
                </segment>
                <segment type="centered" id="3">
                    <points count="2">
                        <p>
                            <x>110</x>
                            <y>70</y>
                            <z>1</z>
                            <r1>3</r1>
                            <r2>4</r2>
                        </p>
                        <p>
                            <x>120</x>
                            <y>60</y>
                            <z>1</z>
                            <r1>3</r1>
                            <r2>4</r2>
                        </p>
```

```xml
        </points>
    <segment type="centered" id="4">
        <points count="1">
            <p>
                <x>60</x>
                <y>40</y>
                <z>1</z>
                <r1>3</r1>
                <r2>4</r2>
            </p>
        </points>
    </segment>
    <segment type="centered" id="5">
        <points count="2">
            <p>
                <x>65</x>
                <y>40</y>
                <z>1</z>
                <r1>3</r1>
                <r2>4</r2>
            </p>
            <p>
                <x>75</x>
                <y>100</y>
                <z>30>
                <r1>3</r1>
                <r2>4</r2>
            </p>
        </points>
    </segment>
</segments>
<paths count="3">
    <path count="2" name="Unknown Path">
        <segment id="1"/>
        <segment id="3"/>
    </path>
    <path count="3" name="Unknown Path">
        <segment id="1"/>
        <segment id="2"/>
        <segment id="4"/>
    </path>
    <path count="3" name="Unknown Path">
```

```
            <segment id="1"/>
            <segment id="2"/>
            <segment id="5"/>
        </path>
    </paths>
</vesseltree>
```

List of Figures

List of Listings

Acronyms

AMF Additive Manufacturing File Format. 24

CFA Curvicircular Feature Aggregation. vii, ix, 3, 5, 43

CPR Curved Planar Reformation. vii, ix, 2

CT Computed Tomography. 1, 7, 8, 13

CTA Computed Tomography Angiography. 1, 5, 11, 13

DSA Digital Subtraction Angiography. vii, ix, 3

JSON JavaScript Object Notation. 19

MinIP Minimum Intensity Projection. 3, 5, 43

MIP Maximum Intensity Projection. 2–5, 43

MRA Magnetic Resonance Angiography. 1, 2, 4, 5, 11

MRI Magnetic Resonance Imaging. 1, 7

PETG polyethylene terephthalate. 7, 36

PLA polylactide. 7, 25

STL STereoLithography. 5, 7, 11, 15, 21, 23, 24, 44

VRML Virtual Reality Modeling Language. 7, 24

VTK Visualization ToolKit. 15, 16, 19, 21, 23

XML EXtensible Markup Language. 18, 19, 21, 24, 39, 44

Bibliography

[1] 3D Hubs Inc. 3D printing materials guide. URL `https://www.3dhubs.com/materials`. [Date accessed: 2016-10-22].

[2] 3D Systems, Inc. What Is An STL File? URL `https://www.3dsystems.com/quickparts/learning-center/what-is-stl-file`. [Date accessed: 2016-11-06].

[3] Autodesk. Netfabb 2017, May 2016. URL `https://www.netfabb.com/`. [Date accessed: 2016-12-07].

[4] T. Auzinger, G. Mistelbauer, I. Baclija, R. Schernthaner, A. Köchl, M. Wimmer, M. E. Gröller, and S. Bruckner. Vessel Visualization using Curved Surface Reformation. *IEEE Transactions on Visualization and Computer Graphics (Proceedings of IEEE Scientific Visualization 2013)*, 19(12):2858–2867, Dec. 2013. URL `https://www.cg.tuwien.ac.at/research/publications/2013/Auzinger_Mistelbauer_2013_CSR/`.

[5] R. R. Baliga, C. A. Nienaber, E. Bossone, J. K. Oh, E. M. Isselbacher, U. Sechtem, R. Fattori, S. V. Raman, and K. A. Eagle. The Role of Imaging in Aortic Dissection and Related Syndromes. *JACC: Cardiovascular Imaging*, 7(4):406–424, 2014. doi: 10.1016/j.jcmg.2013.10.015. URL `http://dx.doi.org/10.1016/j.jcmg.2013.10.015`.

[6] G. Biglino, P. Verschueren, R. Zegels, A. M. Taylor, and S. Schievano. Rapid prototyping compliant arterial phantoms for in-vitro studies and device testing. *Journal of Cardiovascular Magnetic Resonance*, 15(1):2, 2013. ISSN 1532-429X. doi: 10.1186/1532-429X-15-2. URL `http://dx.doi.org/10.1186/1532-429X-15-2`.

[7] N. Bizzotto, I. Tami, A. Santucci, R. Adani, P. Poggi, D. Romani, G. Carpeggiani, F. Ferraro, S. Festa, and B. Magnan. 3D Printed replica of articular fractures for surgical planning and patient consent: a two years multi-centric experience. *3D Printing in Medicine*, 2(1):2, 2016. ISSN 2365-6271. doi: 10.1186/s41205-016-0006-8. URL `http://dx.doi.org/10.1186/s41205-016-0006-8`.

[8] N. Bizzotto, I. Tami, A. Tami, A. Spiegel, D. Romani, M. Corain, R. Adani, and B. Magnan. 3D Printed models of distal radius fractures. *Injury*, 47(4):976 – 978, 2016. ISSN 0020-1383. doi: http://dx.doi.org/10.1016/j.injury.2016.01.013. URL `http://www.sciencedirect.com/science/article/pii/S0020138316000152`.

[9] P. Brown. 3D Printed Cadavers: Ready for Prime Time?, 2014. URL `http://www.medpagetoday.com/PublicHealthPolicy/MedicalEducation/46897`. [Date accessed: 2016-10-27].

[10] C. Buchanan. 3-D Printing Takes Guesswork Out of Tricky Pediatric Heart Surgery, 2014. URL `http://www.whattoexpect.com/wom/baby/0226/3-d-printing-takes-guesswork-out-of-tricky-pediatric-heart-surgery.aspx`. [Date accessed: 2016-10-26].

[11] P. Cignoni and G. Ranzuglia. MeshLab v1.3.3. URL `http://meshlab.sourceforge.net/`. [Date accessed: 2016-12-07].

[12] M. Di Prima, J. Coburn, D. Hwang, J. Kelly, A. Khairuzzaman, and L. Ricles. Additively manufactured medical products – the FDA perspective. *3D Printing in Medicine*, 2(1):1, 2016. ISSN 2365-6271. doi: 10.1186/s41205-016-0005-9. URL `http://dx.doi.org/10.1186/s41205-016-0005-9`.

[13] D. S. Gupta. A New Technique Allows Surgeons to Operate on the Tiniest Patients, 2014. URL `http://www.everydayhealth.com/news/new-technique-allows-surgeons-to-operate-on-the-tiniest-patients/`. [Date accessed: 2016-10-26].

[14] A. Håkansson, M. Rantatalo, T. Hansen, and A. Wanhainen. Patient specific biomodel of the whole aorta - the importance of calcified plaque removal. *VASA. Zeitschrift fur Gefasskrankheiten*, 40(6):453–459, 2011.

[15] T. Halterman. 3D Printed Anatomy Series Released by Monash University: A Medical Training Game Changer, 2015. URL `https://3dprint.com/68721/3d-printed-anatomy-series/`. [Date accessed: 2016-10-28].

[16] T. Heinzeller and C. Büsing. *Histologie, Histopathologie und Zytologie für den Einstieg*. Thieme, 2001. ISBN 9783131268310. URL `https://books.google.at/books?id=n8GKdCfDPwkC`.

[17] R. Herzig, S. Burval, B. Krupka, I. Vlachova, K. Urbanek, and J. Mares. Comparison of ultrasonography, CT angiography, and digital subtraction angiography in severe carotid stenoses. *Eur. J. Neurol.*, 11(11):774–781, Nov 2004.

[18] A. L. Jardini, M. A. Larosa, R. M. Filho, C. A. de Carvalho Zavaglia, L. F. Bernardes, C. S. Lambert, D. R. Calderoni, and P. Kharmandayan. Cranial reconstruction: 3D biomodel and custom-built implant created using additive manufacturing. *Journal of Cranio-Maxillofacial Surgery*, 42(8):1877 – 1884, 2014. ISSN 1010-5182. doi: http:

48

//dx.doi.org/10.1016/j.jcms.2014.07.006. URL `http://www.sciencedirect.com/science/article/pii/S1010518214002303`.

[19] A. Kanitsar, D. Fleischmann, R. Wegenkittl, P. Felkel, and M. E. Gröller. CPR - Curved Planar Reformation. In *IEEE Visualization 2002*, pages 37–44, Oct. 2002. URL `http://www.cg.tuwien.ac.at/research/vis/adapt/`. human contact: kanitsar@cg.tuwien.ac.at.

[20] A. Kanitsar, R. Wegenkittl, D. Fleischmann, and M. E. Gröller. Advanced Curved Planar Reformation: Flattening of Vascular Structures. In *IEEE Visualization 2003*, pages 43–50, Oct. 2003. URL `http://www.cg.tuwien.ac.at/research/vis/adapt/`. human contact: technical-report@cg.tuwien.ac.at.

[21] S. N. Kurenov, C. Ionita, D. Sammons, and T. L. Demmy. Three-dimensional printing to facilitate anatomic study, device development, simulation, and planning in thoracic surgery. *The Journal of thoracic and cardiovascular surgery*, 149(4): 973–979, 2015.

[22] H. Lin, L. Shi, and D. Wang. A rapid and intelligent designing technique for patient-specific and 3D-printed orthopedic cast. *3D Printing in Medicine*, 2(1):4, 2016. ISSN 2365-6271. doi: 10.1186/s41205-016-0007-7. URL `http://dx.doi.org/10.1186/s41205-016-0007-7`.

[23] W. E. Lorensen and H. E. Cline. Marching cubes: A high resolution 3D surface construction algorithm. In *ACM siggraph computer graphics*, volume 21, pages 163–169. ACM, 1987.

[24] MakerBot Industries. File Types. URL `https://support.makerbot.com/learn/3d-printing/3d-printing-terms/file-types_12662#gcode-and-x3gs3g`. [Date accessed: 2016-11-07].

[25] M. Markl, R. Schumacher, J. Küffer, T. A. Bley, and J. Hennig. Rapid vessel prototyping: vascular modeling using 3t magnetic resonance angiography and rapid prototyping technology. *Magnetic Resonance Materials in Physics, Biology and Medicine*, 18(6):288–292, 2005. ISSN 1352-8661. doi: 10.1007/s10334-005-0019-6. URL `http://dx.doi.org/10.1007/s10334-005-0019-6`.

[26] P. G. McMenamin, M. R. Quayle, C. R. McHenry, and J. W. Adams. The production of anatomical teaching resources using three-dimensional (3D) printing technology. *Anatomical sciences education*, 7(6):479–486, 2014.

[27] G. Mistelbauer, A. Morar, A. Varchola, R. Schernthaner, I. Baclija, A. Köchl, A. Kanitsar, S. Bruckner, and M. E. Gröller. Vessel Visualization using Curvicircular Feature Aggregation. *Computer Graphics Forum*, 32(3):231–240, June 2013. URL `https://www.cg.tuwien.ac.at/research/publications/2013/mistelbauer-2013-cfa/`.

[28] D. Mitsouras, P. Liacouras, A. Imanzadeh, A. A. Giannopoulos, T. Cai, K. K. Kumamaru, E. George, N. Wake, E. J. Caterson, B. Pomahac, et al. Medical 3D printing for the radiologist. *RadioGraphics*, 35(7):1965–1988, 2015.

[29] D. Molina. Local doctor hoping to build a "Library of Hearts", 2014. URL `http://peoriapublicradio.org/post/local-doctor-hoping-build-library-hearts`. [Date accessed: 2016-10-24].

[30] M. Moody. Surgeons Begin Using 3D Printing to Help Explain Patients' Conditions to Them, 2014. URL `https://3dprint.com/8306/surgery-3d-printing/`. [Date accessed: 2016-10-23].

[31] National Institutes of Health. 3D Prints in Medicine. URL `http://3dprint.nih.gov/about/medicine`. [Date accessed: 2016-10-23].

[32] National Institutes of Health. What file formats are used in 3D Printing? URL `http://3dprint.nih.gov/faqs/1781`. [Date accessed: 2016-11-06].

[33] Neuroth AG. Besser schützen, länger hören, 2015. URL `http://www.neuroth.at/fileadmin/user_upload/PDFs/150630_HEF_AT_Industiefolder_web.pdf`. [Date accessed: 2016-10-22].

[34] Nevit Dilmen. Saccular aortic aneurysm, 2016. URL `https://3dprint.nih.gov/discover/3DPX-003309`. [Date accessed: 2017-01-27].

[35] M. K. O'Reilly, S. Reese, T. Herlihy, T. Geoghegan, C. P. Cantwell, R. N. Feeney, and J. F. Jones. Fabrication and assessment of 3D printed anatomical models of the lower limb for anatomical teaching and femoral vessel access training in medicine. *Anatomical sciences education*, 9(1):71–79, 2016.

[36] A. S. Rose, C. E. Webster, O. L. Harrysson, E. J. Formeister, R. B. Rawal, and C. E. Iseli. Pre-operative simulation of pediatric mastoid surgery with 3D-printed temporal bone models. *International Journal of Pediatric Otorhinolaryngology*, 79(5): 740 – 744, 2015. ISSN 0165-5876. doi: http://dx.doi.org/10.1016/j.ijporl.2015.03.004. URL `http://www.sciencedirect.com/science/article/pii/S0165587615001159`.

[37] W. Schroeder, K. Martin, and B. Lorensen. VTK - The Visualization Toolkit. *Kitware*, 2004. URL `http://www.vtk.org/`.

[38] M. Schünke, E. Schulte, and U. Schumacher. *Prometheus - LernAtlas der Anatomie: allgemeine Anatomie und Bewegungssystem; 182 Tabellen.* Thieme, 2007.

[39] B. Sevenson. Illinois Doctor is Building a Library of 3D Printable Hearts, 2014. URL `https://3dprint.com/3655/library-3d-printable-hearts/`. [Date accessed: 2016-10-24].

[40] R. Sharma. The 3D printing revolution you have not heard about, 2013. URL `http://www.forbes.com/sites/rakeshsharma/2013/07/08/the-3d-printing-revolution-you-have-not-heard-about/#1024eacc21e1`. [Date accessed: 2016-10-22].

[41] J. L. Silberstein, M. M. Maddox, P. Dorsey, A. Feibus, R. Thomas, and B. R. Lee. Physical models of renal malignancies using standard cross-sectional imaging and 3-dimensional printers: a pilot study. *Urology*, 84(2):268–273, 2014.

[42] The Qt Company. Qt 5.7.0. URL `https://www.qt.io/`. [Date accessed: 2016-12-04].

[43] L. Thomason. TinyXML-2. URL `http://www.grinninglizard.com/tinyxml2/`. [Date accessed: 2016-12-03].

[44] J. Velut. vtkKinship. URL `https://github.com/jeromevelut/vtkKinship`. [Date accessed: 2016-12-03].

[45] N. Wake, H. Chandarana, W. Huang, S. Taneja, and A. Rosenkrantz. Application of anatomically accurate, patient-specific 3D printed models from MRI data in urological oncology. *Clinical Radiology*, 71(6):610 – 614, 2016. ISSN 0009-9260. doi: http://dx.doi.org/10.1016/j.crad.2016.02.012. URL `http://www.sciencedirect.com/science/article/pii/S0009926016000878`.

[46] Wikipedia. VRML. URL `https://en.wikipedia.org/wiki/VRML`. [Date accessed: 2016-11-07].

[47] S.-J. Yoo, O. Thabit, E. K. Kim, H. Ide, D. Yim, A. Dragulescu, M. Seed, L. Grosse-Wortmann, and G. van Arsdell. 3D printing in medicine of congenital heart diseases. *3D Printing in Medicine*, 2(1):3, 2016. ISSN 2365-6271. doi: 10.1186/s41205-016-0004-x. URL `http://dx.doi.org/10.1186/s41205-016-0004-x`.